İSTANBUL UNIVERSITY CERRAHPAŞA

ORIGINAL ARTICLE
Electrica 2024; 24(3): 574-588

Field Weakening Operation of Pentagon Connected FPIM Under Open Phase Fault With Electric Vehicle Load

Jahera Shaik, Chudamani R, Chandani P Gor

Sardar Vallabhbhai National Institute of Technology, Surat, Gujarat, India

Cite this article as: Jahera S, Chudamani R. and C. P. Gor, "Field weakening operation of pentagon connected FPIM under open phase fault with electric vehicle load," *Electrica*, 24(3), 574-588, 2024.

ABSTRACT

Electric vehicles (EVs) are now becoming a reliable option in transport applications. Multi-phase machines, having advantages over their three phase counterparts, are gaining attention in the recent times. This paper investigates the comprehensive field weakening operation (FWO) of pentagon connected five phase induction machines (PC-FPIM) with electric vehicle as load application. The pentagon connection is chosen as it is superior to that of star in terms of attaining lower copper loss and obtaining maximum achievable torque. The PC-FPIM along with EV load, is run up to more than 1.5 times that of its rated speed which indicates that the drive is operating in constant power region (CPR). The rapid increase of acceleration/deceleration of the vehicle enables the machine to exceed its thermal loading limits. Consequently, a discussion on derating is articulated in which a simple yet effective trial and error-based technique is proposed to ensure the safe thermal loading capability of the machine. Thus, the dynamic model of electric vehicle fed PC-FPIM is presented and an appropriate fault tolerant control strategy (FTCS) is applied to restore balance to the system. The simulations are carried out in "MATLAB, Simulink (MathWorks, Natick, Massachusetts, USA)" and the results supported the aforementioned statements.

***Index Terms*—**Electric vehicle load, fault tolerant control strategy, field weakening operation and derating, five phase induction machine, open phase fault modeling

I. INTRODUCTION

Depletion of natural resources is the primary concern behind the boom of electric vehicles in transportation [1]. As they offer robustness and reliability, EV manufacturers are showing tremendous interest as it boosts power autonomy. Electric vehicles can be powered by different machines like Induction Machines, Permanent Magnet Synchronous Machines, DC Machines, and Switched Reluctance Machines. Multi-phase induction machines are gaining popularity among these machines because of the benefits they provide, such as high tolerance to faults, high torque density, reduced torque ripple, and reliable operation. Among multi-phase machines, five-phase induction motors have a simpler design and a lower number of power electronic components. Hence, the five-phase induction motor is considered. Induction motors have been used in industrial applications for decades and are well-understood by engineers and manufacturers. This familiarity can simplify the development process and reduce risks associated with adopting newer technologies. While IPMSMs offer certain advantages in terms of efficiency and power density, induction motors remain a viable choice for four-wheeler EVs, particularly in applications where cost, reliability, and simplicity are prioritized.

Operating these machines for the entire speed range of the vehicle is a herculean task. To operate the machine beyond the base speed, one of the primitive solutions is to weaken the flux and operate the machine in the constant power region. The role of multi-phase machines in driving electric vehicle applications is presented in [2], [3]. Conversely, the impact of increasing the number of phases for electromagnetic machines, which do require a wide variety of power electronic converters, is investigated; thus, providing a comparative analysis between a standard three-phase design and a nine-phase design. The results feature the enhancement of torque quality. The performance of a five-phase permanent magnet synchronous motor for EV load is presented in [4] where a space vector modulation control strategy is used to drive the five-phase PMSM.

Corresponding author:
Jahera Shaik

E-mail:
jahe100@gmail.com

Received: June 24, 2023

Revision Requested: April 12, 2024

Last Revision Received: April 29, 2024

Accepted: June 11, 2024

Publication Date: July 24, 2024

DOI: 10.5152/electrica.2024.23087

In [5], dynamic performance of a five-phase interior permanent magnet (IPM) motor for series hybrid EV applications is presented. To operate the machine throughout a wide speed range, a vector control strategy based on the SVPWM approach is implemented. The design of a five-phase IPM for electric vehicle application is presented in [6]. This study evaluated the torque and speed capabilities of the five-phase IPM to the three-phase IPM. Furthermore, a novel PM motor drive with high power density for EVs is presented in [7]. FEM analysis is employed to carry out the analysis for the design and optimization of the proposed motor. Two new topologies of IPM for EV applications are presented in [8]. The advantages of multi-phase machines were explored using an open-end winding dual inverter drive. This literature provides some insights into multiphase for electric vehicle applications.

The field weakening operation of IPM motors is described in [9], where both axially laminated and radially laminated multiple barrier rotors were built and tested. The flux weakening of permanent magnet machines from a machine perspective is presented in [10]. Various design approaches are discussed in this paper. The operation of IPMSM with EV load application using different control strategies is presented in [11-15]. Another field weakening approach is proposed for IPMSM for EV applications in [16], where the field weakening control of fast dynamics and variable DC link voltage is achieved by a suitable combination of a lookup table and voltage feedback controller. Very few literature works are available on the field weakening operation of multi-phase induction machines, whereas abundant work is done on the three-phase induction machine side in this aspect. This work focuses on the field weakening approach of a five-phase induction machine connected in a pentagon configuration with the EV application as load. Under open phase fault, the pentagon connection is deemed superior to star as it attains lower stator copper loss and larger torque capability, as discussed in [17].

The main contributions of this article are: (i) Integration of EV load with pentagon connected five-phase induction machine (PC-FPIM) is done in both healthy and an open phase fault conditions. (ii) The machine is operated in both the constant power region and the field weakening region, thus exploring the entire speed range of the drive. (iii) A simple yet effective trial-and-error-based derating technique is introduced to reinstate phase currents. This is done by limiting the speed to a certain extent and by using acceleration and deceleration limiters as tapering the torque is no longer a tenable option.

The FPIM can be used in three different configurations, i.e., star, pentagon, and pentacle configurations. In this work, the pentagon-connected FPIM is selected as the propulsion machine for the electric vehicle. This paper is grouped into four sections. In Section II, a detailed description of the modeling of FPIM and fault is presented. Also, the Fault Tolerant Control Strategy (FTCS) is discussed briefly. Field Weakening Operation (FWO) along with the EV load is discussed in Section III. Section IV outlines Simulink results, followed by the conclusion in section V.

II. FPIM MODELING – OPEN PHASE FAULT MODEL

The mathematical model of a five-phase machine is akin to that of a three-phase machine in an arbitrary reference frame. The transformation matrix of the five-phase machine differs from that of the three-phase machine and is shown in (2). The first two rows of the matrix define $\alpha\beta$ components, last row defines the standard zero-sequence component, and the remaining two rows define two-dimensional orthogonal planes *xy* whose components are the projections of the original space (phase variables) onto the new reference frame. The transformation's *dq* components account for basic torque and flux generation. In this case, the additional *xy* components are totally decoupled and do not contribute to torque generation. The fundamental torque and flux production are accounted for by only *dq* components of the transformation in a symmetrically distributed FPIM. The squirrel cage induction motor (SCIM) with a short-circuited rotor is employed in this article. The correlation between actual components and arbitrary reference frame components is given by

$$F_{\alpha\beta xy0} = K_t F_{abcde} \tag{1}$$

where K_t is the Clarke transformation matrix.

$$\boldsymbol{K_t} = \sqrt{\frac{2}{5}} = \begin{bmatrix} 1 & \cos\gamma & \cos 2\gamma & \cos 3\gamma & \cos 4\gamma \\ 0 & \sin\gamma & \sin 2\gamma & \sin 3\gamma & \sin 4\gamma \\ 1 & \cos 2\gamma & \cos 4\gamma & \cos 6\gamma & \cos 8\gamma \\ 0 & \sin 2\gamma & \sin 4\gamma & \sin 6\gamma & \sin 8\gamma \\ \sqrt{0.5} & \sqrt{0.5} & \sqrt{0.5} & \sqrt{0.5} & \sqrt{0.5} \end{bmatrix}; \text{where } \gamma = \frac{2\pi}{5} \tag{2}$$

The transformation of stator variables to the synchronous reference frame is done by using

$$\begin{bmatrix} F_{ds} \\ F_{qs} \end{bmatrix} = \begin{bmatrix} \cos\theta & -\sin\theta \\ \sin\theta & \cos\theta \end{bmatrix} \begin{bmatrix} F_{\alpha s} \\ F_{\beta s} \end{bmatrix} \tag{3}$$

The expression for the electromagnetic torque in terms of arbitrary reference frame variables in power-invariant form is given as

$$T_e = P\left(\frac{L_m}{L_r}\right)\left(\Psi_{dr} i_{qs} - \Psi_{qr} i_{ds}\right) \tag{4}$$

The torque equilibrium equation is given by

$$J\frac{d\omega_r}{dt} T_e - T_L - B\omega_r \tag{5}$$

The state-space model of the five-phase induction motor is illustrated below.

$$\frac{d}{dt}\begin{bmatrix} I_{ds} \\ I_{ds} \\ \Psi_{dr} \\ \Psi_{qr} \end{bmatrix} = \mathbf{A}\begin{bmatrix} I_{ds} \\ I_{qs} \\ \Psi_{dr} \\ \Psi_{qr} \end{bmatrix} + \mathbf{B}\begin{bmatrix} V_{ds} \\ V_{qs} \end{bmatrix} \tag{6}$$

where $\mathbf{A} = \begin{bmatrix} -a_1 & \omega_e & a_2 & Pa_3\omega_r \\ -\omega_e & -a_1 & Pa_3\omega_r & a_2 \\ a_5 & 0 & -a_4 & \omega_{sl} \\ 0 & a_5 & -\omega_{sl} & -a_4 \end{bmatrix}; \mathbf{B} = \begin{bmatrix} c & 0 \\ 0 & c \\ 0 & 0 \\ 0 & 0 \end{bmatrix}; a_1 = \frac{1}{\sigma L_s}\left(R_s + R_r\frac{L_m^2}{L_r^2}\right);$

$$a_2 = \frac{1}{\sigma L_s} R_r \frac{L_m^2}{L_r^2}; a_3 = \frac{1}{\sigma L_s}\frac{L_m}{L_r};$$

$$a_4 = \frac{R_r}{L_r}; a_5 = \frac{R_{rL_m}}{L_r}; \omega_e - P \quad \omega = \omega_{sl}; c = \frac{1}{\sigma L_s}$$

where the *qs, ds, dr,* and *qr* subscripts correspond to *d* and *q* axes quantities of stator and rotor respectively. The other terms involved are: ½ denotes flux linkage, ω_e denotes the speed of the reference frame, ω_r denotes the mechanical speed of the rotor in r/s, P denotes pole pairs, r_s and r_γ denote the resistance/phase of stator and rotor of the motor, respectively; the other terms represent the conventional notations.

A. Pentagon Connection – Single Phase Open

An open phase stator fault is modeled by adopting the back-EMF technique. The back-EMF for the faulty phase is computed and applied as the source voltage during the occurrence of the fault for that specific phase, while the remaining phases receive the supply from the inverter. Phase "*a*" is deemed faulty in this article. The representation of the phase and line currents for this connection is shown in Fig. 1. The currents i_a, i_b, i_c, i_d, and i_e represents line currents where as $i_{ab}, i_{bc}, i_{cd}, i_{de}$, and i_{ea} represents phase currents. To establish the relation between the line and phase currents, apply KCL at all the nodes to obtain the following equations. Applying KCL at nodes a, b, c, d, and e.

$$i_a = i_{ab} - i_{ea};\quad i_b = i_{bc} - i_{ab};\quad i_c = i_{cd} - i_{bc};\quad i_d = i_{de} - i_{cd};\quad i_e = i_{ea} - i_{de}$$

The association between phase and line currents in a PC-FPIM is given as follows.

$$\begin{bmatrix} i_a \\ i_b \\ i_c \\ i_d \\ i_e \end{bmatrix} = \boldsymbol{S} \begin{bmatrix} i_{ab} \\ i_{bc} \\ i_{cd} \\ i_{de} \\ i_{ea} \end{bmatrix} where\, \boldsymbol{S} = \begin{bmatrix} 1 & 0 & 0 & 0 & -1 \\ -1 & 1 & 0 & 0 & 0 \\ 0 & -1 & 1 & 0 & 0 \\ 0 & 0 & -1 & 1 & 0 \\ 0 & 0 & 0 & -1 & 1 \end{bmatrix} \quad (7)$$

This matrix that is connecting line and phase currents is represented by *S***.** During a fault scenario, one of the phases is disconnected, say, phase *ab* is disconnected, hence $i_{ab}=0$. Substituting this condition in the above equations, the new set of equations during the fault are given below,

$$i_a = -i_{ea};\quad i_b = i_{bc};\quad i_c = i_{cd} - i_{bc};\quad i_d = i_{de} - i_{cd};\quad i_e = i_{ea} - i_{de}$$

As phase "*a*" is at fault, it is not possible for the zero sequence currents to flow through the open delta connection. During the fault condition, *S* is replaced by S_f where S_f represents the matrix during the fault condition.

$$\boldsymbol{S}_f = \begin{bmatrix} 0 & 0 & 0 & 0 & -1 \\ 0 & 1 & 0 & 0 & 0 \\ 0 & -1 & 1 & 0 & 0 \\ 0 & 0 & -1 & 1 & 0 \\ 0 & 0 & 0 & -1 & 1 \end{bmatrix}$$

The current flowing through the faulty phase becomes zero, i.e., $i_{ab}=0$. Generally, in a star connection the sum of all the currents is zero, irrespective of the inverter supply during fault conditions. However, in pentagon connected FPIM, the behavior of the machine during a fault is influenced by the inverter supply. Hence, there is a scope for adjusting the voltages of the inverter. Utilizing this advantage, the inverter supply is controlled such that the currents hold a specific relation, which is elaborated in the next subsection. By incorporating these conditions, the rest of the phase currents (remaining four healthy phases) become balanced, producing constant MMF. Besides producing balanced MMF, the summation of all the phase currents is zero. In situations where there is no provision to control the inverter supply in closed-loop operation, the sum of all the phase currents is non-zero. The assumption that the sum of all the phase currents is forced to zero leads to the condition below.

$$i_{xs} = -i_{\alpha s} \quad (8)$$

This condition is substituted to obtain the following relation:

$$V_{xs} = -r_s i_{\alpha s} - \frac{d}{dt} L_{ls} i_{\alpha s} \quad (9)$$

The obtained expression above is substituted for $V_{\alpha s}$ and the following relation can be obtained:

$$V_{\alpha s} = \sqrt{\frac{2}{5}} \left(F_{bs} - F_{cs} - F_{ds} + F_{es}\right)\left(\cos\gamma + \cos 2\gamma\right) - \left(r_s i_{\alpha s} + \frac{d}{dt}\left(L_{ls} i_{\alpha s}\right)\right) \quad (10)$$

The unknown voltage across phase, '*a*' i.e., its back-EMF, is calculated as

$$V_{backemf} = -\left(V_{bc} + V_{ea}\right)\cos 2\gamma - \left(V_{cd} + V_{de}\right)\cos\gamma - \sqrt{\frac{5}{2}}\left(r_s i_{\alpha s} + \frac{d}{dt}\left(L_{ls} i_{\alpha s}\right)\right) \quad (11)$$

The criteria used to ensure the accuracy of the single-phase open fault model are: $i_{ab}=0$, $i_b=i_{bc}$, $i_a=-i_{ea}$. The results pertaining to the open-phase fault are discussed in detail further.

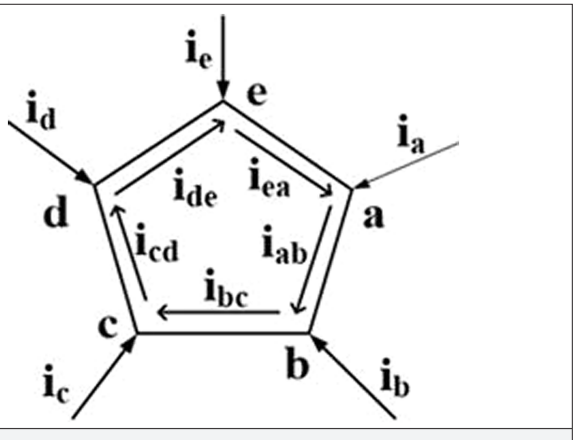

Fig. 1. Pentagon connection.

B. Fault Tolerant Control Strategy

Although it is essential to retain the same rotational MMF even under fault conditions, the approach to accomplish this is not unique. With an FPIM under an open phase fault, however, four phase currents are accessible that need to be regulated. The approach is clearly not unique with two equations and four unknowns. It is advisable to have a set of currents that will create the same rotating MMF with the smallest feasible current magnitude for all phases for an optimal solution. One such approach is discussed to obtain this result [18]. The MMF expression in an FPIM is given below.

$$MMF = Ni_{ab} + aNi_{bc} + a^2 Ni_{cd} + a^3 Ni_{de} + a^4 Ni_{ea} \quad (12)$$

where $a = 1 \angle 72^{\circ}$. Under generalized conditions, the five currents form a balanced positively rotating set given by

$$MMF = \frac{5NI}{2} e^{j\theta} \tag{13}$$

The real and imaginary parts of (13) are

$$\frac{5NI}{2} e^{j\theta} = N\left(i'_{bc} + i'_{ea}\right)\cos 72^0 - N\left(i'_{cd} + i'_{de}\right)\cos 36^0 \tag{14}$$

$$\frac{5NI}{2} e^{j\theta} = N\left(i'_{bc} + i'_{ea}\right)\sin 72^0 - N\left(i'_{cd} - i'_{de}\right)\sin 36^0 \tag{15}$$

It is extremely acceptable to suppose the below relation to maintain an undisturbed rotating MMF.

$$i'_{bc} = -i'_{de} \tag{16}$$

$$i'_{cd} = -i'_{ea} \tag{17}$$

Consequently, the following can be determined:

$$i'_{bc} = i'_{de} = 1.38i\cos\left(\omega t + \varphi - 36^0\right) \tag{18}$$

$$i'_{cd} = i'_{ea} = 1.38i\cos\left(\omega t + \varphi - 144^0\right) \tag{19}$$

Therefore, when one of the four phases fails to operate, the currents in the other four phases manage to provide the torque to FPIM without the addition of zero-sequence current. The phasor given in Fig. 2. depicts the currents of the remaining phases during a fault. In this case, the current amplitude rises to a value that is only 38% larger than when all five phases are operational.

A mathematical model of the FPIM drive in the open phase fault is constructed, and a pertinent Fault Tolerant Control Strategy (FTCS) is applied to the system to decrease torque ripple during the fault. The reference currents for the hysteresis current controller are generated by altering the *xy* components without impacting the Indirect Field Oriented Control (IFOC). Fig. 3 depicts the overall block diagram of the system. The FTCS applied is also shown in Fig. 3. An outer speed loop with a discrete PID controller is incorporated, from which i_{qref} is generated. In the design of a discrete PID speed controller, the trial and error method is adopted. The speed response obtained with the proportional gain (K_p) equal to 1.4, the integral gain (K_i) equal to 2.2, and the derivative gain (K_d) equal to 1 is deemed as being satisfactory.

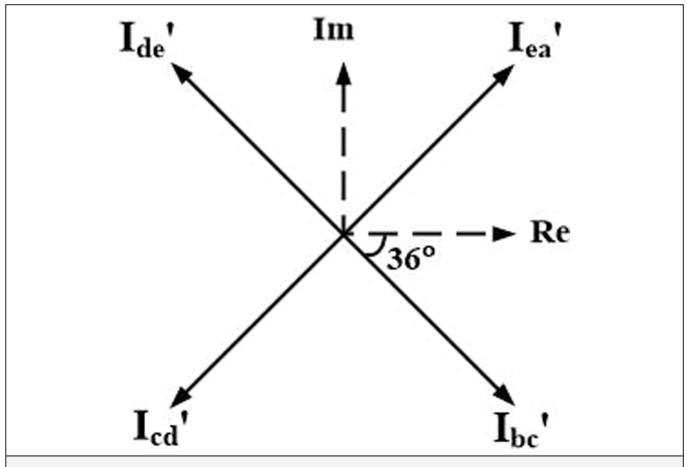

Fig. 2. Phasor diagram of desired currents for the remaining four healthy phases.

As one phase current vanishes, the machine experiences an unbalanced effect. The remaining phase currents increase in magnitude and can exceed their rated values. Also, the torque ripple shoots up, which is quite undesirable. The distortion in *αβ* currents is accounted for by *xy* currents to provide ripple-free torque during post-fault scenarios. The following relation is obtained by using the conditions from (16), (17) and using the transformation matrix from (2).

$$i^*_{xs} = -i^*_{\alpha s}; \quad i^*_{ys} = -0.263 i^*_{\beta s} \tag{20}$$

III. FIELD WEAKENING OPERATION WITH EV AS LOAD

A. Field Weakening Operation

In various applications such as servo, traction, space application vehicle drives, and high-speed operation of machines is required. Generally, to drive high speed EVs, the machine should be customized such that the constant power region is 4–5 times the constant torque region. To operate the machine at high speeds, the flux of the machine can be easily weakened by reducing the flux component of current corresponding to Indirect Field Oriented Control (IFOC). The conventional flux-weakening technique is adopted in this article. Rotor flux reference is varied in proportion to the inverse of rotor speed, ω_r. If the polarity of i^*_{qs} is negative, the slip speed will become negative, which will shift the rotor position below the d^r axis. The speed control range in IFOC can be easily extended from standstill to the field-weakening region. The changes that can be made to generate i_{ds} and i_{qs} references in achieving IFOC so that the considered FPIM can operate in the field-weakening region are depicted in Fig. 3. As the drive cycle is used as reference speed, the machine switches between the constant torque region and constant power region according to the variations in speed. As per the Fig. 3., rated flux will be present in the air gap, which is 1.27 Wb in the constant torque region. When the machine operates with more than the rated speed, the flux value changes as per the machine parameters.

B. Electric Vehicle Dynamics

Vehicle dynamics is often divided into three broad categories.

(i) Longitudinal dynamics is the study of a vehicle's response in a straight line, including acceleration, braking, etc. (ii) Lateral dynamics discusses the investigation of a moving vehicle. (iii) Vertical dynamics provides information about how a vehicle will behave when traveling vertically and running into obstacles like speed bumps and puddles, among others.

In accordance with Newton's second law of motion, the acceleration of the vehicle can be given by:

$$\frac{dV}{dt} = \frac{\sum F_t - \sum F_r}{Mass} \tag{21}$$

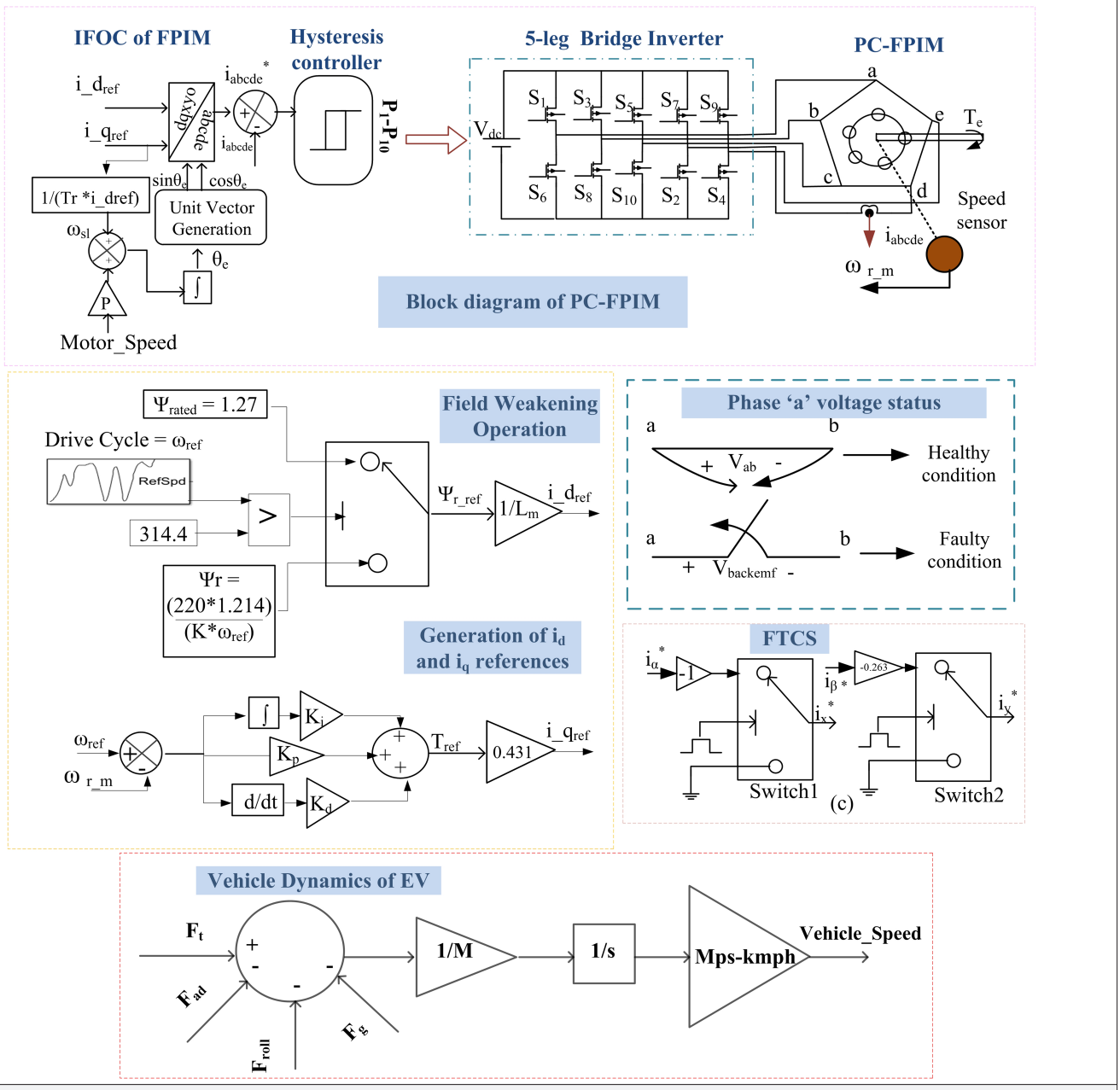

Fig. 3. Block diagram of PC-FPIM including Field weakening operation and FTCS for EV load.

where V is vehicle speed, F_t is the overall tractive force of the vehicle, and F_r is the composite resistive forces acting on the vehicle. The vehicle dynamic equation can be obtained as:

$$F_t = F_g + F_{roll} + F_{ad} + Ma = Mg\sin\alpha + Mg(C_0 + C_1 v) + \frac{1}{2}\rho C_d A_F (v - v_w)^2 + \left(M + \frac{J_{wh}}{r^2}\right)\frac{d\omega}{dt} \quad (22)$$

The resistive forces are discussed below.

1. *Grading Resistance:* As the vehicle moves up/down, its weight component produces opposition, which is known as grading force, usually called grading resistance, and is expressed as,

$$F_g = Mg\sin\alpha \quad (23)$$

where α is the angle of grade, g is the natural acceleration.

2. *Rolling Resistance:* The force produced by the hysteresis effect in tyres during the forward shift is called the rolling resistant moment. In order to balance this rolling resistive moment and keep thetyremoving, a force, F_{roll}, operating on the hub of the wheel is needed.

$$F_{roll} = Mgr_f\cos\alpha;\quad r_f = 0.01*\left(1+\frac{v}{160}\right) \quad (24)$$

where r_f is the rolling coefficient, and α is the road angle. This equation accurately predicts the values of r_f at speeds up to 128 km/h.

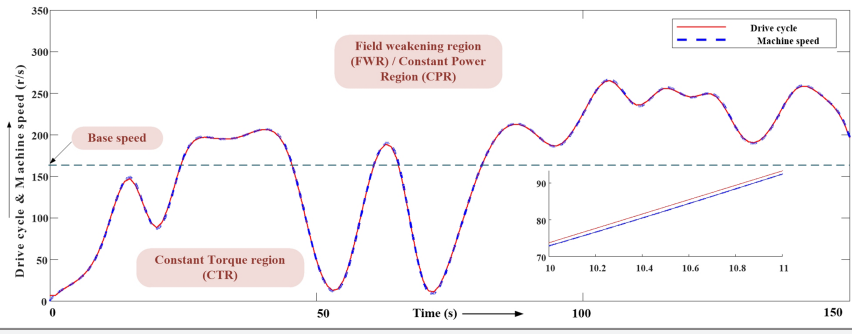

Fig. 4. Transient drive cycle as reference vs machine actual speed.

3. *Aerodynamic Drag:* Aerodynamic drag is the force that opposes the motion of the vehicle in the air moving at a certain speed. It is mostly caused by two factors: shape drag and skin friction. The expression for aerodynamic drag is given as:

$$F_{ad} = \frac{1}{2}\rho C_d A_F \left(v - v_w\right)^2 \tag{25}$$

where C_d is the aerodynamic drag coefficient, v_w is the component of the wind speed in the vehicle moving direction. For detailed information on EV modeling, [19] can be referred to.

IV. RESULTS AND DISCUSSION

A drive cycle of a custom data set is considered as the reference speed, according to the Indian urban road scenario representing road driving conditions in Surat city. The peak speed of the drive cycle is 31 km/hr. The drive cycle is a combination of both below and above base speeds. Hence, the FPIM enters into the constant power region (CPR) from the constant torque region (CTR) and vice versa as long as the driving is ON. The performance of the drive with the EV as its load is discussed in two subsections, with the former one being the healthy scenario and the latter being the open phase fault scenario. The parameters of the PC-FPIM chosen for the EV load are presented in Table I, and the parameters of the electric vehicle chosen are presented in Table II.

A. Healthy Condition

The drive cycle as the reference speed and the vehicle's actual speed are shown in Fig. 4. This figure shows the machine speed tracking the reference speed, which is the drive cycle with a custom data set. The constant torque region and constant power region are marked in the figure where the below base speed region is termed as CTR and the above base speed region as CPR. The current drawn by the machine is affected by the acceleration of the vehicle. For instance, if the vehicle gets stuck in traffic, the speed slowly goes to zero. As soon as the green light is on, the driver needs to pick up speed where the acceleration should be raised, thereby causes more current to flow in the windings (probably more than rated). Therefore, derating of currents should be done, which is explained thoroughly further. The rated peak current of the considered FPIM is 3.1 A per phase. The profile of the current space vector, $\overline{I_s}$ which is the vector sum of all the five-phase currents, is shown in Fig. 5. The zoomed version of the five-phase currents throughout the drive cycle is also shown in Fig. 5. It is evident from the figure that the five-phase currents have a phase difference of 72°. The torque produced by the machine, T_e and the torque required by the wheel T_{wheel} are shown in Fig. 6b. The difference in the two signals can be attributed to Bω, which gives the loss due to viscous friction. In the field weakening region, the machine speed increases at the expense of reduced torque. If the magnetic flux is weakened by reducing the i_{ds} current, back emf is reduced and more stator current is drawn. The rated value of i_{ds} is 3.025 A, and during field weakening operation, the detailed profile is given in Fig. 6a.

B. Fault Condition

An open phase fault is created in the "*a*" phase of the PC-FPIM driving the electric vehicle load. As the drive cycle is set as a reference, acceleration and deceleration of the vehicle take place as per the custom data set. So, there are two possibilities of fault occurrence that are presented in this work.

TABLE I. PC-FPIM PARAMETERS

$S = 2\ HP$	$R_s = 10\ \Omega$	$L_m = 0.42$ H
$V_{ph} = 220$ V	$R_r = 6.3\Omega$	$B = 0.008$
$I_{ph} = 2.1$ A	$L_s = 0.46$ H	$J = 0.03$
$f = 50$	$L_r = 0.46$ H	$P = 2$

TABLE II. ELECTRIC VEHICLE PARAMETERS

Air Density	1.225 kg/m^3
Aero Drag Coefficient, C_d	0.44
Frontal Area	2 m^2
Mass	350 kg
Rolling Resistant Coefficient, C_0	0.01
Rolling Resistant Coefficient, C_1	625×10^{-7}
Gravity	9.8 m/s^2
Inclination Angle	0
Motor Maximum Torque	16 Nm
Braking Torque	5 Nm
Wheel Radius	0.305 m
Drive Spin Loss, Gear Ratio	0.5 Nm, 9:1

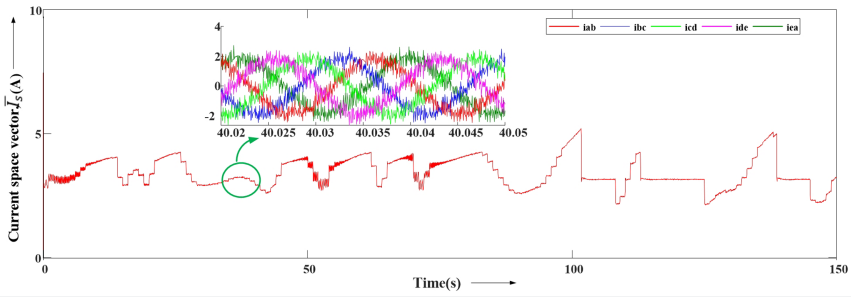

Fig. 5. Current space vector under healthy condition (zoomed version of the five-phase currents shown inside).

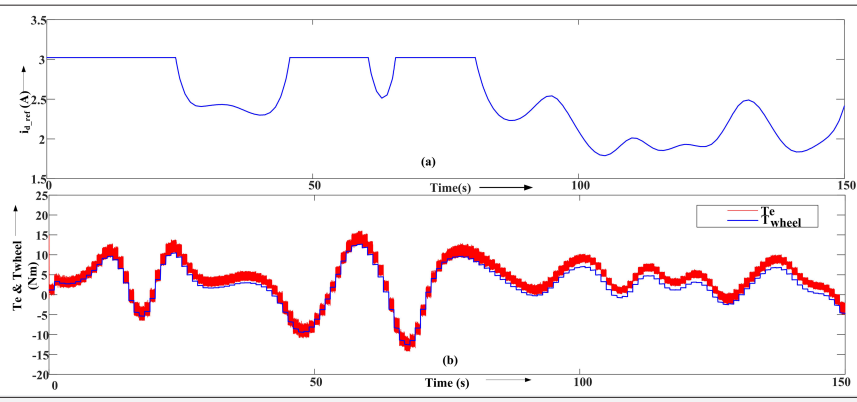

Fig. 6. i_{ds} current and torque profile in healthy condition.

i. Fault occurs when the acceleration is at its maximum.
ii. Fault occurs when the vehicle is maintaining a constant speed for a while, i.e., during steady speed.

A brief analysis is presented in both scenarios backed up by the simulation results.

Case (i): An open phase fault is created at 24 s, where the acceleration is at its maximum. The phase currents drawn are more compared to the healthy condition scenario. At 25 s, the fault-tolerant control strategy discussed earlier is applied to balance the system. The transition of currents from healthy to a fault state is shown in Fig. 7. (upper portion), and the transition of currents during and after applying FTCS is shown in Fig. 7 (lower portion). As one phase is blacked out, a disturbance and asymmetry are created in the remaining four phases. The relation of the line currents i_a and i_b with the phase currents i_{ea} and i_{bc} (fault check points) is shown in Fig. 8. respectively. The i_{as} and i_{xs} currents hold the relation as illustrated in Fig. 8. It is noticed from the simulation results that after the application of FTCS, balance is restored to the system.

Case (ii): The same open phase fault is created at 30 s, which is approximately the steady speed of the vehicle for a while. As the fault occurs, the ripple in the electromagnetic torque produced by the machine shoots up and is reinstated after applying FTCS. This observation can be depicted in Fig. 9. In this case, the fault is created at 30 s, and FTCS is applied at 31 s, and the machine continues to run with the fault for the rest of the time. The phase currents are shown in Fig. 10. This figure has zoomed versions that show the transition from a healthy to fault state and also the transition from a fault to a post-fault state. After the application of FTCS, the phase currents are seen to be balanced. It is evident that the fault created during

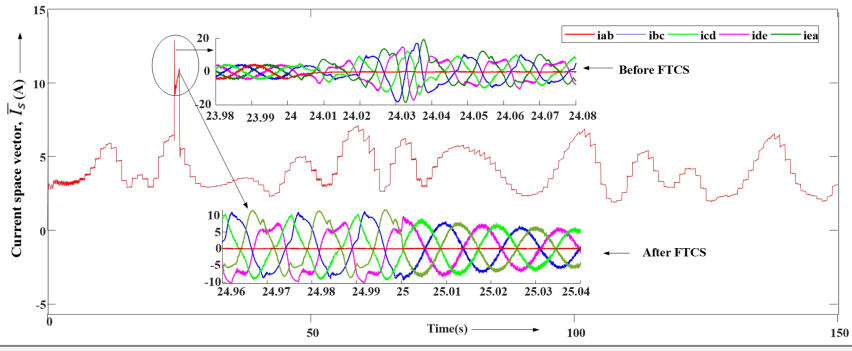

Fig. 7. Case (i) Phase currents when the acceleration is at its maximum.

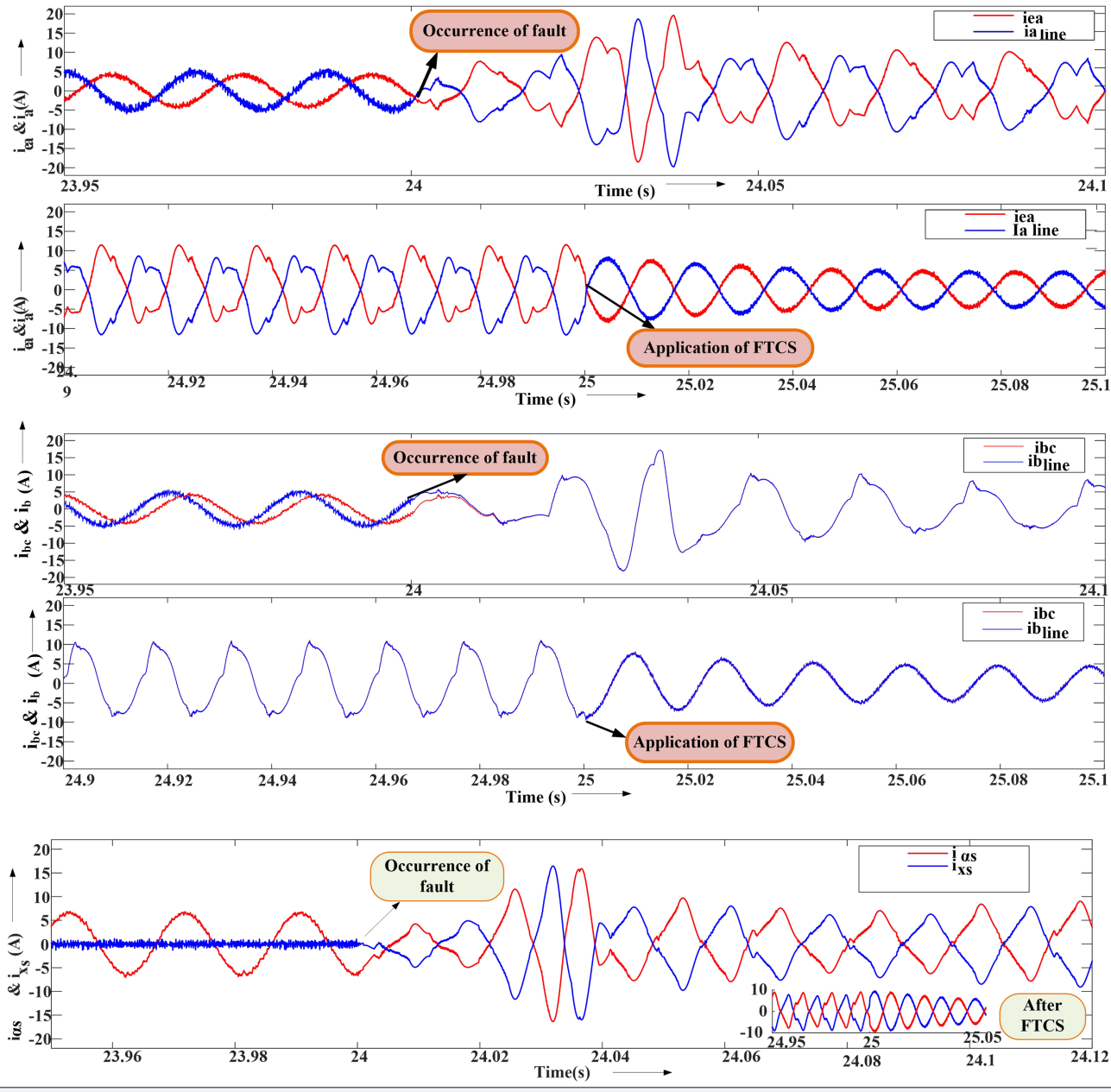

Fig. 8. Fault check points validating the fault model.

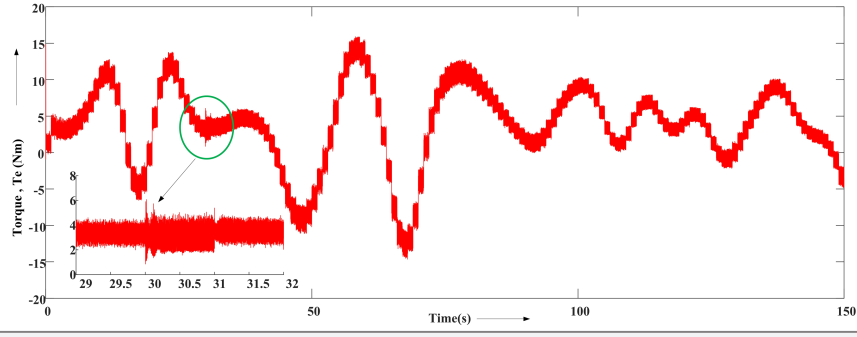

Fig. 9. Reduction in torque ripple after FTCS.

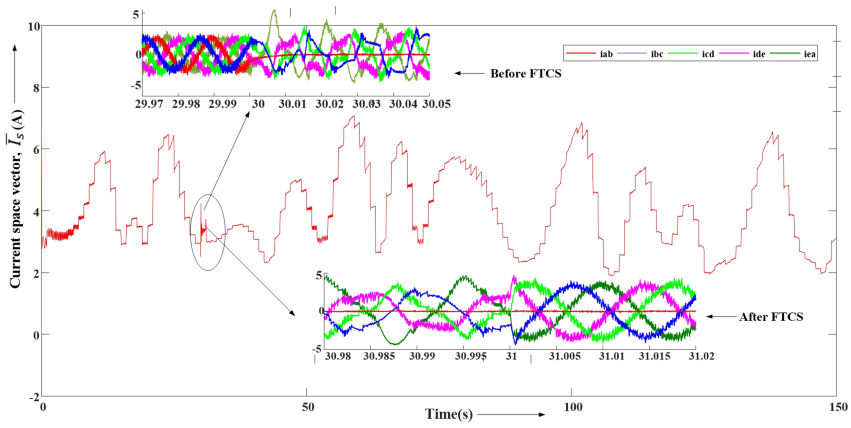

Fig. 10. Case (ii) phase currents when the fault is created in steady state.

the maximum acceleration point draws more current compared to the fault during steady speed. Either way, the machine is required to operate within its thermal loading limit, agreeing to the need for derating. An elaborate discussion is articulated on the application of derating in the coming section.

C. Trajectories of Stator Currents

The electromagnetic torque is developed by the stator current space vectors interacting with the rotor field, comprising even the torque ripple. When the electromagnetic torque is purely the average torque, this interaction results in a circular trajectory. Likewise, when the torque has a low-frequency ripple component dominated by a negative sequence component, the interaction results in an elliptical trajectory. No torque is produced when the current space vectors from spatial planes interact, whereas the interaction of current space vectors spinning at various speeds on the same spatial plane produces torque ripple. This phenomenon can be observed in Fig. 11.

D. Derating

As the FPIM is operated in the field weakening region with one phase open-circuited, the currents are too high for the machine to be safe. Operation of the machine under adverse conditions inevitably requires derating to safeguard the machine from overheating. Derating should be applied in both healthy as well as fault conditions. Two possible factors contribute to the derating of the machine currents. They are (a) $\Delta\omega$ factor and (b) Δacc factor. The EV operates until the point where the machine can supply enough accelerating torque. After that point, the speed will deviate from the drive cycle, resulting in sluggish response. A critical limit on the speed of the drive cycle produces favorable results. A critical limit of 25 km/h is applied on the drive cycle, which reduces the magnitudes of phase currents to some extent. Also, setting a critical limit on the speed of the drive cycle alone is not sufficient to maintain the currents in the desired band. The crucial point for the increase in currents is the acceleration with which the EV is driven. If the acceleration is limited, the desired criteria are met. Here comes the Δacc factor into the picture. Different limits are suggested for different cases for better operation of the drive in both in healthy and fault conditions. Fig. 12 explains the derating technique using $\Delta\omega$ factor and Δacc factor through flowchart representation, and the derating logic applied is depicted in Fig. 13. With the occurrence of the fault, the machine's thermal conditions are at stake. To ensure this, the current needs

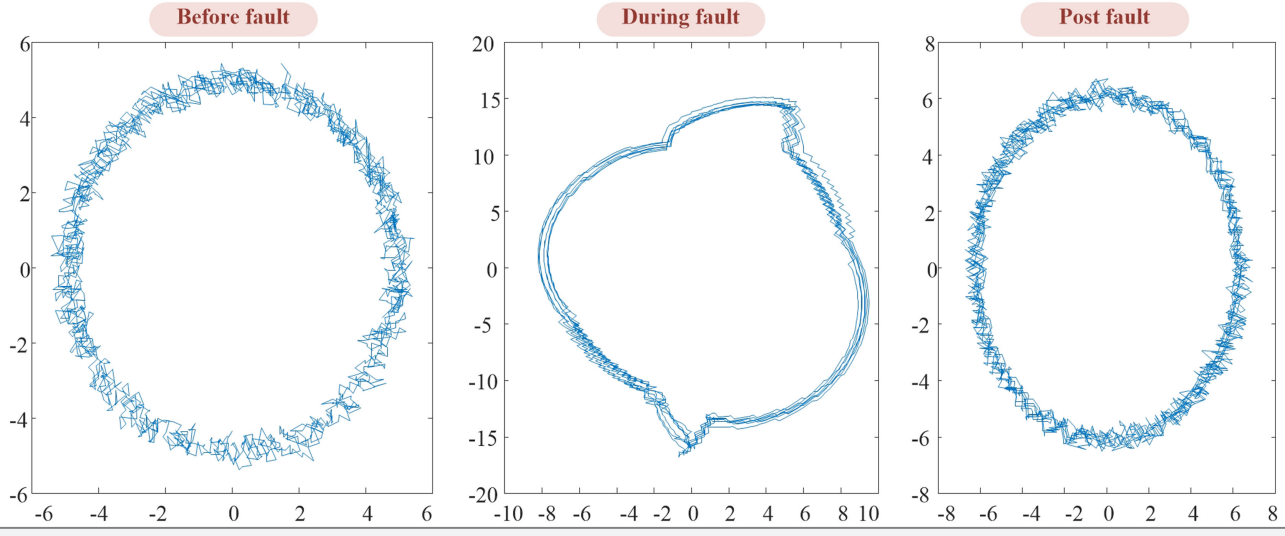

Fig. 11. Trajectories of current space vector in various cases.

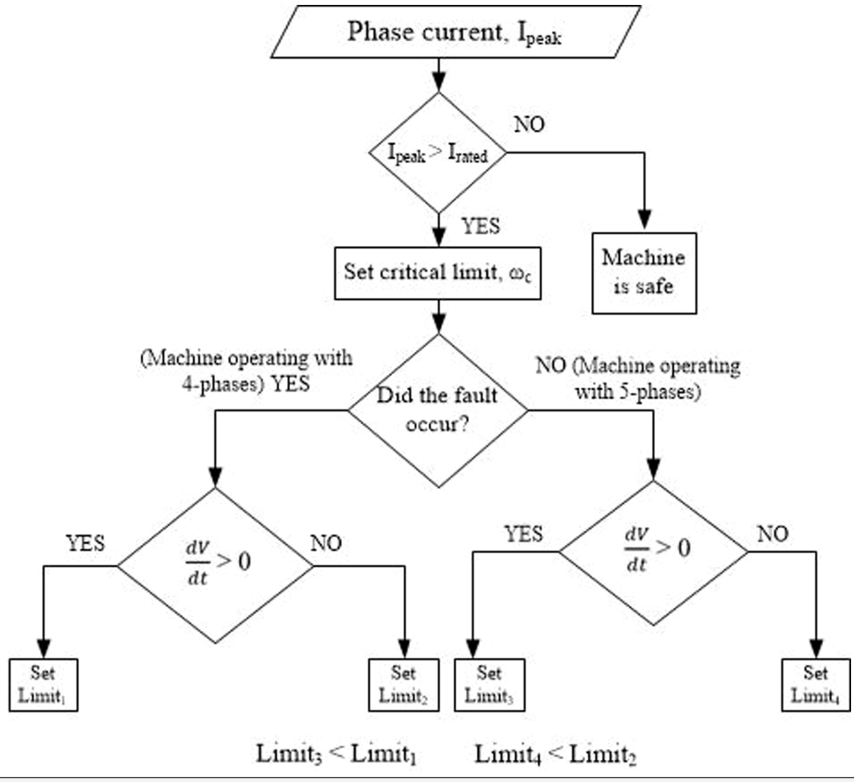

Fig. 12. Flowchart of derating technique.

to be checked in both in healthy and faulty conditions. Firstly, peak current is observed during the healthy condition. If it exceeds the rated value, a critical limit on speed should be applied; otherwise, no further modifications are needed as the machine is considered safe. After the occurrence of the fault, check for *dv/dt* value. If it is positive, i.e., the machine is accelerating, then set a limiter to bring the currents within the rated value. If the machine is decelerating, set a different limit as mentioned in Fig. 13. The same logic is repeated for the healthy condition case as well. The rate at which the machine is accelerating is mainly responsible for the increase in currents. That is the reason for considering *dv/dt* as the prime factor for derating. The simulation results after the application of derating are shown in Fig. 14a–c. Fig. 14a shows the stator current space vector without any derating. At 100 s, the critical limit on speed is applied, which results in reduced currents as shown in Fig. 14b. Even after the application of a critical limit on speed, the magnitude of the currents does not get reduced below the rated value. Therefore, a limit on acceleration, i.e., *dv/dt* is also applied, and the currents are shown in Fig. 14c.

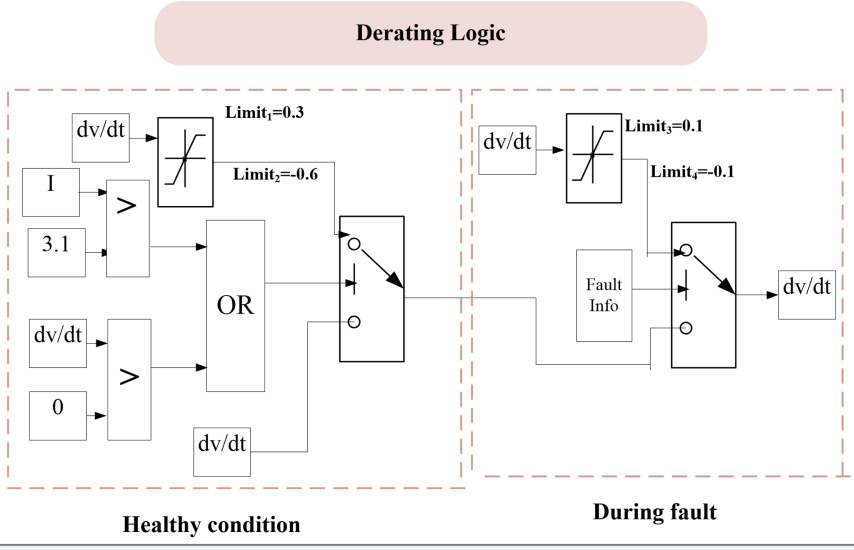

Fig. 13. Derating logic.

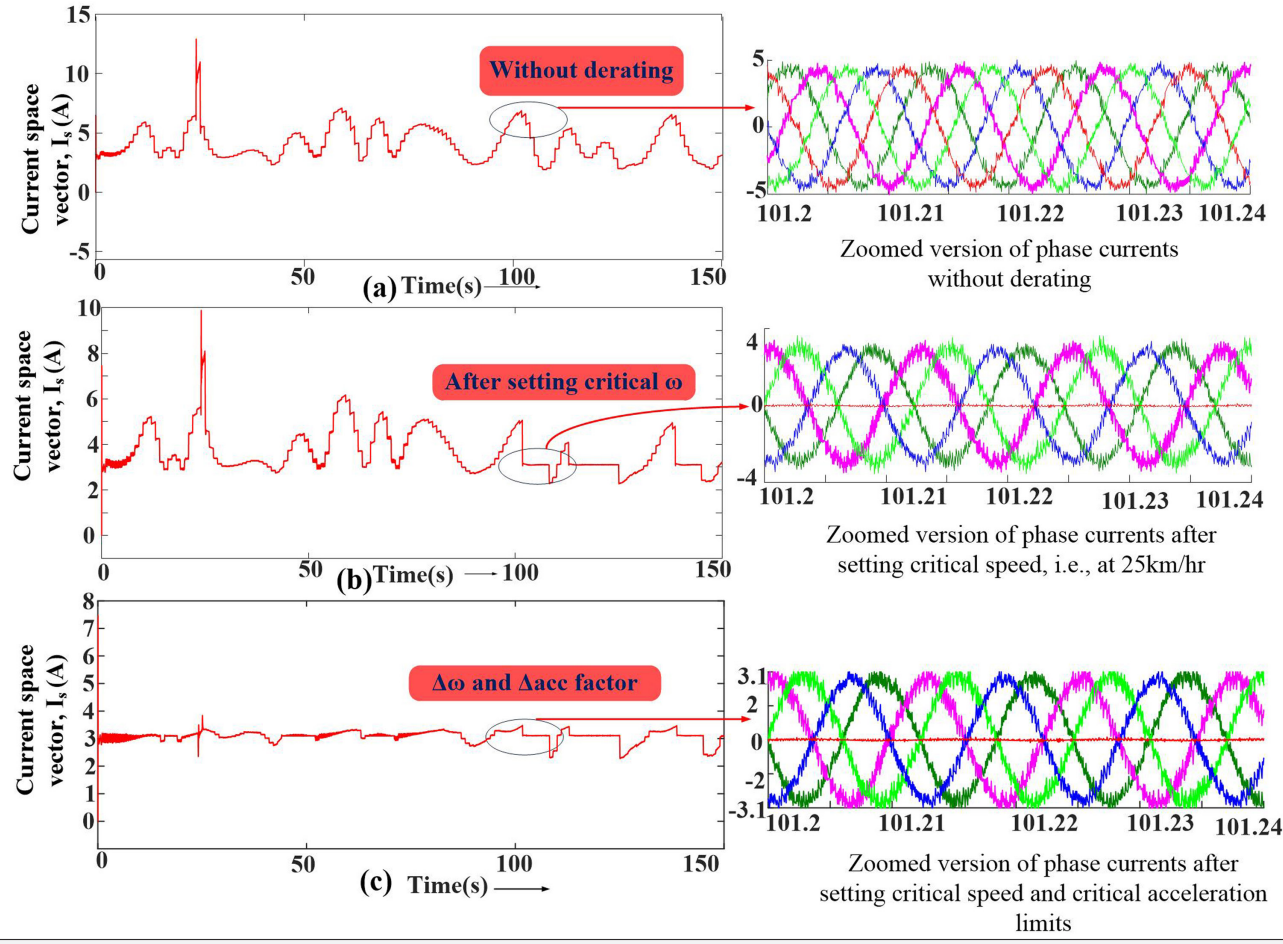

Fig. 14. Derating of phase currents using trial and error approach.

The zoomed versions of all the five-phase currents are shown on the right side of each figure. The maximum power delivered during constant hp operation after the application of derating is the same as the rated power which is 1119 W. The plot between output power (W) vs Vehicle speed (kmph) is shown in Fig. 15.

E. Performance of the Drive with Different Drive Cycles

This drive with EV load can operate for any drive cycle effectively in closed loop. The EPA Urban Dynamometer Driving Schedule (UDDS) is usually called the "LA4" or "the city test" and indicates driving conditions of a city. Considering this UDDS, the speed of the machine vs UDDS is shown in Fig. 16. The Torque profile is shown in Fig. 17. The current space vector is depicted in Fig. 18. where the five-phase currents are shown in a zoomed version. The same FTCS and the derating logic work effectively for this drive cycle also. One more drive cycle is tested: NEDC, new European drive cycle. This test cycle includes accelerating and slowing down several times as well as driving at steady speeds and with the engine idling. The speed of the machine vs NEDC is shown in Fig. 19. The electromagnetic torque produced is shown in Fig. 20. The current space vector with

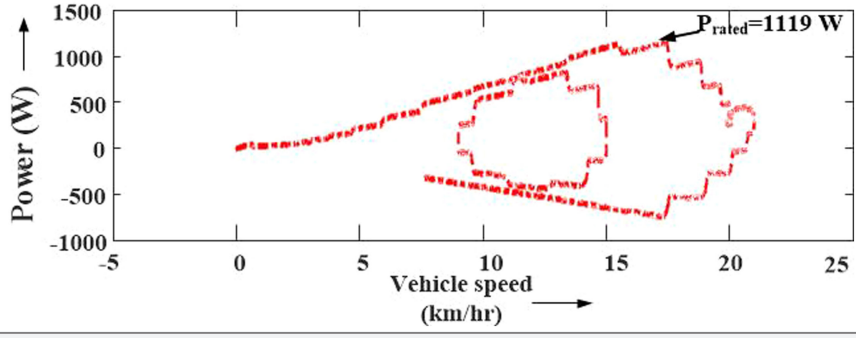

Fig. 15. Output power vs vehicle speed.

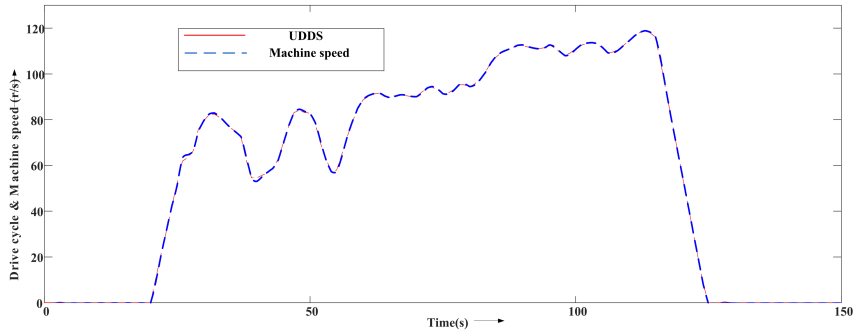

Fig. 16. UDDS drive cycle as reference vs machine actual speed.

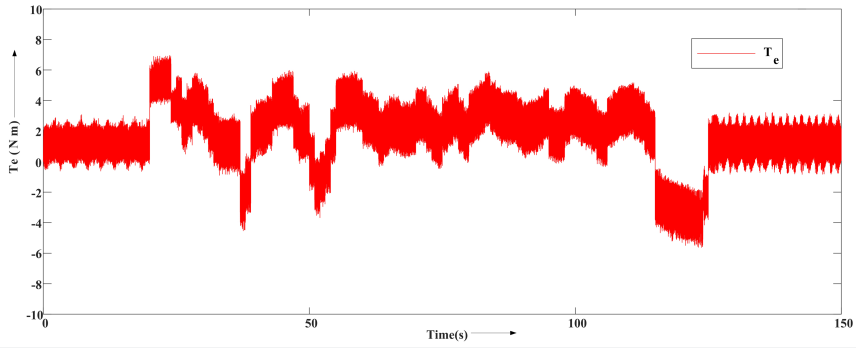

Fig. 17. Torque profile with UDDS.

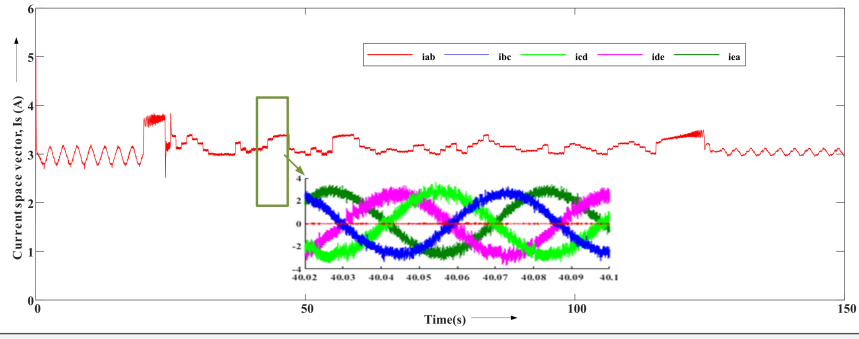

Fig. 18. Current space vector (zoomed version of the five-phase currents shown inside) for UDDS.

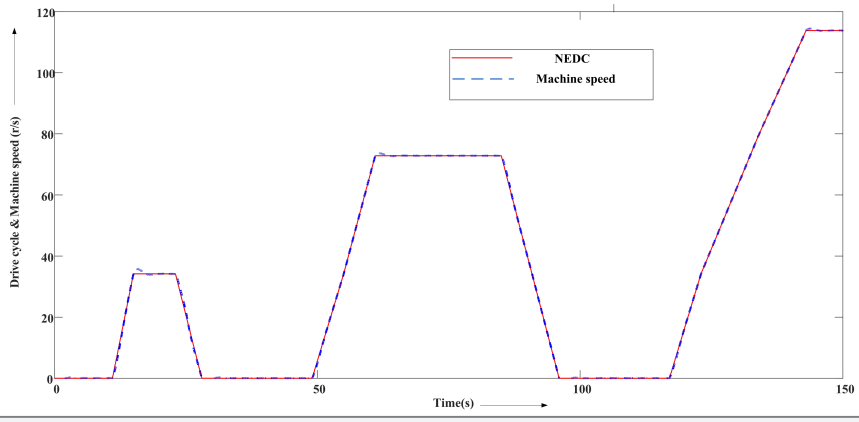

Fig. 19. NEDC vs machine actual speed.

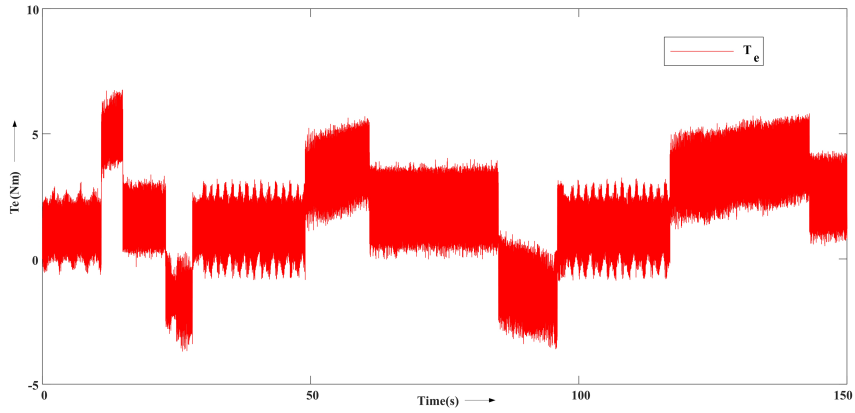

Fig. 20. Torque profile with NEDC.

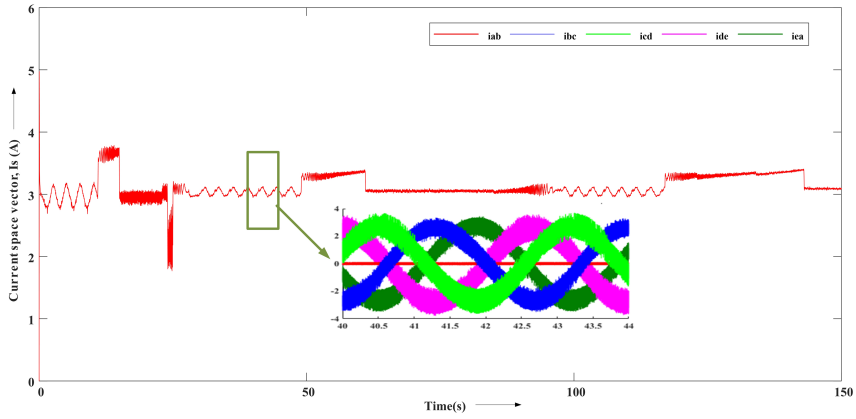

Fig. 21. Current space vector (zoomed version of the five-phase currents shown inside) for NEDC.

a zoomed version of phase currents is presented in Fig. 21. These phase currents are very well maintained within the thermal loading capability of the machine after the application of derating logic. The operation of the drive with NEDC as a reference works effectively during fault conditions as well.

V. CONCLUSION

In this study, the field weakening operation of PC-FPIM with an electric vehicles as load application is presented. Here, the machine is operated over the entire speed range, i.e., below and above the base speeds. The rated speed of the PC-FPIM is 19.15 km/h. This machine is operated at 1.5 times the rated speed in healthy and fault conditions. An open phase fault is introduced into the system, modeled, and mitigated using a suitable FTCS to balance the remaining four phases. The chosen FTCS effectively reduces the torque ripple and helps in operating with the four remaining phases. The natural tendency of the drive cycle includes accelerating, slowing down, driving at a steady speed for a while, and sometimes, idling. These random variations in the drive cycle affect the current ratings of the machine. Hence, a detailed discussion on derating is presented, which is necessary to maintain the thermal loading limit of the machine. A trial-and-error-based derating is applied both in healthy and faulty conditions. The discussions are substantiated by the simulation results in the MATLAB/Simulink environment.

Availability of Data and Materials: The data that support the findings of this study are available on request from the corresponding author.

Peer-review: Externally peer-reviewed.

Author Contributions: Concept – J.S., R.C., C.G.; Design – J.S., R.C., C.G.; Supervision – R.C., C.G.; Resources – N.I.L.; Materials – N.I.L.; Data Collection J.S., R.C., C.G.; and/or Processing – J.S., R.C., C.G.; Analysis and/or Interpretation – J.S., R.C., C.G.; Literature Search – J.S.; Writing – J.S., R.C., C.G.; Critical Review – J.S., R.C., C.G.

Declaration of Interests: The authors have no conflict of interest to declare.

Funding: The authors declared that this study has received no financial support.

REFERENCES

1. R. Kene, T. Olwal, and B. J. van Wyk, "Sustainable Electric Vehicle Transportation" *Sustainability*, vol. 13, no. 22, p. 12379, 2021. [CrossRef]
2. J. Riveros, B. Bogado, J. Prieto, F. Barrero, S. Toral, and M. Jones, "Multiphase machines in propulsion drives of electric vehicles," *Proceedings of 14th International Power Electronics and Motion Control Conference EPE-PEMC*, vol. 2010. IEEE Publications, 2010, pp. T5–201.
3. N. Schofield, X. Niu, and O. Beik, "Multiphase machines for electric vehicle traction," in 2014 IEEE Transportation Electrification Conference and Expo (ITEC), IEEE Publications, 2014, pp. 1–6. [CrossRef]
4. A. Hezzi, S. Ben Elghali, Y. Ben Salem, and M. N. Abdelkrim, "Control of five-phase PMSM for electric vehicle application," in 2017 18th

International Conference on Sciences and Techniques of Automatic Control. and Computer Engineering (STA), 2017. IEEE PUblications, pp. 205–211.
5. S. Sadeghi and L. Parsa, "Design and dynamic simulation of five phase interior permanent magnet machine for series hybrid electric vehicles," in IEEE Green Technologies Conference, Vol. 2010. IEEE PUBLICATIONS, 2010, pp. 1–6.
6. O. Beik, R. Yang, and A. Emadi, "Design of a 5-phase IPM machine for electric vehicles," in IEEE Transportation Electrification Conference and Expo (ITEC), Vol. 2018. IEEE PUBLICATIONS, 2018, pp. 168–172.
7. C. C. Chan, J. Z. Jiang, G. H. Chen, X. Y. Wang, and K. T. Chau, "A novel polyphase multipole square-wave permanent magnet motor drive for electric vehicles," *IEEE Transactions on Industry Applications*, vol. 30, no. 5, pp. 258–1266, 1994.
8. L. Zhang, Y. Fan, R. D. Lorenz, A. Nied, and M. Cheng, "Design and comparison of three-phase and five-phase FTFSCW-IPM motor open-end winding drive systems for electric vehicles applications," *IEEE Trans. Veh. Technol.*, vol. 67, no. 1, pp. 385–396, 2017.
9. W. L. Soong and N. Ertugrul, "Field-Weakening Performance of Interior Permanent-Magnet Motors," *IEEE Transactions on Industry Applications*, vol. 38, no. 5, 2002, pp. 1251–1258.
10. T. A. Lipo, "Field weakening of permanent magnet machines--design approaches, in *Proc. EPEPEMC*. Citeseer, 2004, pp. 1–7.
11. Z. Huang, C. Lin, and J. Xing, "A parameter-independent optimal field-weakening control strategy of IPMSM for electric vehicles over full speed range," *X, IEEE Trans. Power Electron.*, vol. 36, no. 4, pp. 4659–4671, 2020. [CrossRef]
12. Y. Wang, J. Wu, Z. Guo, C. Xie, J. Liu, and X. Jin, "Flux-weakening fuzzy adaptive ST-SMO sensorless control algorithm for PMSM in EV," *X.* C. a. L. J. a, *J. Supercomput.*, vol. 78, no. 8, pp. 10930–10949, 2022. [CrossRef]
13. Y. Zhang, W. Chang, and Y. Liang, "High dynamic response control method of pmsm in field weakening region for electric vehicle," 2022, pp. 2414–2419. [CrossRef]
14. Q. Huang, Q. Huang, H. Guo, and J. Cao, "Design and research of permanent magnet synchronous motor controller for electric vehicle," *Energy Science & Engineering*, vol. 11, no. 1, pp. 112–126, 2023. [CrossRef]
15. A. Dalal, and M. Sreejeth, "Wide speed Range control of PMSM based on MTPA and flux-weakening control," International Conference on Power, Instrumentation, Control and Computing, Vol. 2023. PICC, 2023, pp. 1–6.
16. J. H. Lee, J. H. Lee, J. H. Park, and C. Y. Won, "Field-weakening strategy in condition of DC-link voltage variation using on electric vehicle of IPMSM," 2011 International Conference on Electrical Machines and Systems, vol. 2011. IEEE Publications, pp. 1–6.
17. A. G. Yepes, J. Doval-Gandoy, F. Baneira, and H. A. Toliyat, "Comparison of stator winding connections in multiphase drives under healthy operation and with one open converter leg" *IET Electr. Power Appl.*, vol. 14, no. 4, pp. 584–596, 2020. [CrossRef]
18. J.-R. Fu and T. A. Lipo, "Disturbance-free operation of a multiphase current-regulated motor drive with an opened phase," *IEEE Trans. Ind. Appl.*, vol. 30, no. 5, pp. 1267–1274, 1994. [CrossRef]
19. M. Ehsani, Y. Gao, and A. Emadi, "E. K. Ehsani, Modern electric, hybrid electric, and fuel cell vehicles." Boca Raton, United States of America: CRC press, 2018.

Jahera Shaik received the B.Tech. degree in Electrical Engineering from RVR & JC college of engineering, Acharya Nagarjuna University, India, in 2013, M.Tech. degree (Power electronics and drives) from Lakireddy Balireddy college of Engineering, JNTUK, India in 2015. Currently, she is pursuing Ph.D. in Electrical Engineering at Sardar Vallabhbhai National Institute of Technology, Surat, Gujarat, India. Her areas of interest are multi-phase machines, Electric vehicles, Power converters and their applications.

R. Chudamani received the B.E. degree in Electrical Engineering from the National Institute of Technology, Surat, India, in 1990, M.Tech. degree (power electronics) in electrical engineering from IIT, Delhi, India, in 1997, and the Ph.D. degree in electrical engineering from IIT, Madras, India, in 2009. She is currently serving as a Professor in the Department of Electrical Engineering, Sardar Vallabhbhai National Institute of Technology, Surat, Gujarat, India, and she has been active in the areas of teaching and research. Her research interests include the areas of power electronics drives, active power filters and multi-phase drives.

Chandani P Gor was born in Baroda, India. She received the B.E. Degree in Electrical Engineering from S.V. National Institute of Technology, Surat, India in 2003, M.E. Degree in Electrical Engineering from Maharaja Sayajirao University of Baroda, Gujarat, India in 2006 and the Ph.D. Degree in Electrical Engineering from Sardar Vallabhbhai National Institute of Technology, Surat, Gujarat, India in 2022. She has been working as an Assistant Professor in the Department of Electrical Engineering of Sardar Vallabhbhai National Institute of Technology, Gujarat, India since 2007. Her research activities are related to Electric vehicles, multi-phase drives and artificial intelligent control techniques.